

A Possible Thin Disk-Wind Launching Mechanism of Broad-line Emission in AGN Applied to Quasar 3C 273

KIRK LONG (ADVISED BY JASON DEXTER)¹

¹*University of Colorado Boulder*

ABSTRACT

Following on the work of [Chiang & Murray \(1996\)](#) we explore how a thin accretion disk with large velocity gradients can act as a mechanism to explain the broad-line region (BLR) in active galactic nuclei (AGN). These large velocity gradients within the disk are an example of what we might expect if there were a wind being driven off of the disk, and we fit this simplified “disk-wind” model to previously published GRAVITY data of Quasar 3C 273. This fit is contrasted against the fit given by the standard “cloud” model ([GRAVITY Collaboration et al. 2019](#)), which yields statistically significant differences in both the assumed size of the BLR as well as the mass of the central supermassive black hole—our fit favors a smaller BLR size and lower black hole mass than previously published. Our fit favors higher inclinations, however—in disagreement with the observed jet orientation in 3C 273 ([Kundt & Gopal-Krishna 1986](#))—indicating the existing “cloud” model fit is preferred, although this “disk-wind launching” model may still better fit other systems. This motivates future study of the dynamical processes that can produce these cloud distributions, as well as further comparison between the two models with a larger population of AGN.

Keywords: GRAVITY, disk-wind, thin disk, 3C273, broad-line region, AGN

1. BACKGROUND

One of the most fascinating astrophysical discoveries of the last century was the observation that quasars show a remarkable degree of line-broadening, with line-widths on the order of thousands of kilometers per second—widths assumed to be caused by the extreme gravity of the central supermassive black hole ([Peterson 2006](#)). The region where these broad lines originate—aptly named the “broad-line region” (BLR)—is assumed to be at distances of $\sim 10^3 - 10^4 r_s$ from the central black hole, inferred by measuring time lags between changes in the continuum (assumed to originate from very near the black hole in the hot central accretion disk) and the BLR line profiles (see [Zhang et al. \(2019\)](#) for a recent study of this phenomenon in quasar 3C 273). While this distance to the BLR is relatively well constrained the geometry and physics governing the BLR is an area of active research, with several disparate models being considered ([Peterson 2006](#)).

Quasars are highly luminous, and while the large central luminosity of these systems is usually assumed to originate from accretion onto their central supermassive black holes ([Rees \(1984\)](#), [Lynden-Bell \(1969\)](#), [Shakura & Sunyaev \(1973\)](#)), it is unclear how far this disk geometry extends. While the geometric picture is simplest if

we assume a thin disk extended as far as the broad-line region, such a disk under ordered rotation with just Keplerian shears should produce a Doppler broadened line profile that is double peaked, which is not observed in the steady state. As shown by [GRAVITY Collaboration et al. \(2019\)](#), the single peak in the line profile can be adequately explained by instead assuming a puffy “cloud” model—assuming that the quasar is seen at low inclinations, with random chaotic motions of puffed up parcels of cold and dense atomic gas responsible for the emission. Such conditions are physically unintuitive (i.e. what is acting to support the vertical extent of the clouds?) and further complicate the assumed geometry of the quasar system. An alternative model first put forward by [Chiang & Murray \(1996\)](#) (hereafter CM96) demonstrated that a single peak could be obtained in the line profile if an extended thin disk was assumed to have high velocity gradients driven by shears in addition to the naively expected Keplerian shear—CM96 specifically considered the addition of radial shearing to the expected Keplerian shearing and assumed the system was seen at high inclinations to generate their single peaked line profiles. This model keeps the simplest geometric picture of an extended thin disk, and there is significant observational evidence for the presence of winds

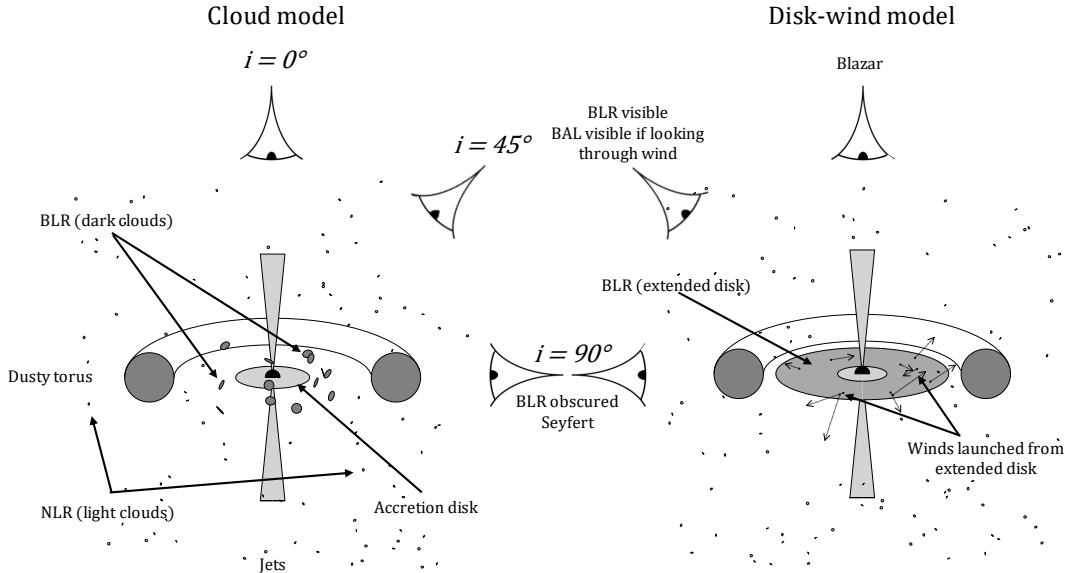


Figure 1. A general (not to scale) overview of the inferred structure of AGN. The narrow line region (NLR) lies at the farthest distances, while the broad absorption and emission line regions (BAL and BLR, respectively) are closer to the black hole. The differences between the “cloud” model that is fit in [GRAVITY Collaboration et al. \(2019\)](#) and the disk-wind launching model considered in this work are shown, with the left panel showing representative darker “clouds” of atomic gas that are between the dusty torus and accretion disk, whereas the right panel replaces these clouds with a broader thin-disk with velocity gradients responsible for the broad-line emission. Note that the velocity gradients drawn here are random, and are just representative possibilities for the many different orientations a wind could be launched from the disk.

in quasars ([Bottorff et al. \(1997\)](#), [Elvis \(2000\)](#), [Hamann et al. \(1993\)](#)), which could be launched by the large velocity gradients in this model. Figure 1 illustrates the general geometry of AGN and the difference between the two models.

Understanding the geometry that governs the broad-line region is critical to inferring system properties such as the mean BLR size and the black hole mass. For example, reverberation mapping techniques allow us to measure a characteristic time delay t between changes in the continuum of the source and changes in the line profile, giving a characteristic size for the BLR of $R \approx ct$ assuming the change is propagated at the speed of light c ([Peterson 2006](#)). The width of the observed line profile then provides a characteristic velocity ΔV , and we can combine these to infer the central mass of the black hole as:

$$M = f \frac{R(\Delta V)^2}{G} \quad (1)$$

G is the gravitational constant and f is the “virial coefficient”—which originates from assuming that the BLR is virialized and whose value is model dependent

on both the geometry and kinematics of the BLR. The notation here matches what is given in [Waters et al. \(2016\)](#). There can be significant measurement uncertainties in both ΔV and t , with measurements of t often influenced by an assumed model-dependent form of the transfer function (discussed and derived later in this work). Thus it is of critical importance to constrain what physical models best fit the BLR.

With the advent of interferometry we can constrain the centroids and phase of the line emission in addition to the line profile, and we see in data collected by GRAVITY that there is clear evidence for ordered rotation around quasar 3C 273 (i.e. see figure 1 of [GRAVITY Collaboration et al. \(2019\)](#) or figure 4 here). Of course if a thin-disk were responsible for BLR emission we would expect to see this sort of ordered rotation, but as shown by [GRAVITY Collaboration et al. \(2019\)](#) the data is also consistent with a distribution of puffed up clouds at large scale heights seen at low inclinations. While the cloud model fits are good, it has not been considered if a thin disk-wind launching model similar to the one first presented in CM96 can also explain the data, an impor-

tant step in determining which model more accurately represents the physics of the BLR. Given the evidence for winds being launched from the BLR the disk-wind launching model is tantalizing in its potential to unify broad-line features seen in AGN under one physical explanation, but we must first extend the model considered by CM96 to all inclination regimes and generate model centroids and phase profiles to compare to the data taken by GRAVITY.

As in CM96, we utilize the Sobolev (Sobolev 1957) approximation in modelling the line emission, as the macroscopic motion of gas within the disk is much larger than the intrinsic line width. The Sobolev optical depth is proportional to the inverse of the line of sight velocity gradient, which in this work is modelled as various possible shears within the thin disk geometry. In the high optical depth limit within the Sobolev regime the equation of radiative transfer is essentially dominated by the source function multiplied by the probability that a photon will escape the disk, which in this limit is directly proportional to the line of sight velocity gradient. Thus, any anisotropic terms present in the velocity gradients of the hydrodynamic thin disk can alter the morphology of the observed line profile, leading to a variety of interesting possible shapes outside of the expected double peak.

2. METHODS

We will take the following assumptions in considering this model for the disk and its associated emission:

1. The disk is geometrically thin, such that we can vertically average it, making the problem \sim two-dimensional only.
2. The disk dynamics are governed by Keplerian rotation with high velocity gradients, such that the associated Sobolev optical depth is high ($\tau \gg 1$), with these gradients being the result of hydrodynamical shearing.
3. All of these velocity gradients are positive—essentially modelling the beginning of an outflowing wind—with their strengths derived assuming that particles are quickly accelerated to the local escape velocity.
4. The continuum is produced very near the black hole and radiates with spherical symmetry, with the amount of incident radiation received at any point in the surrounding disk falling off as $1/r^2$. The disk then reprocesses this incident radiation to create the emission line we model, with variability timescales set by the geometry.

The Sobolev approximation relies on the key assumption that characteristic size of the region “local” $s_0 = v_t |\frac{dv_t}{dr}| \approx R (\frac{v_t}{v})$ to any emitting parcel of gas is much smaller than the overall size of the system. When the velocity gradients are large there will be a corresponding shift in the resonance frequencies of emitting and absorbing atoms, and thus the size scale at which atoms at a point within the medium can radiatively interact is determined by this characteristic size s_0 . As shown in CM96, in using the Sobolev approximation the intensity emitted at any point in the disk relies on the line of sight velocity gradient $\frac{dv_t}{dr}$, and we can use this approximation when $s_0 \ll R$. From CM96 we also know that the characteristic size of the BLR is on the order of $10^3 r_s$. At these distances simple models of thin accretion disks show the temperature should be of order $10^3 - 10^4 K$ (depending upon the size of the black hole and the accretion rate as shown in Sagiv et al. (2014)), thus we can estimate the thermal speed $v_t \approx \sqrt{\frac{2kT}{m}} \approx 10 \text{ km/s}$. The observed line profile is broadened to widths of thousands of km/s, and thus the Sobolev approximation is valid.

In the Sobolev approximation we can calculate the frequency dependent line profile from a steady continuum source L_ν as:

$$L_\nu = \sin i \int r dr \int_0^{2\pi} d\phi k(r) \beta(r, \phi, i) S(r) \delta[\nu - \tilde{\nu}(\phi, r)] \quad (2)$$

This relationship was first shown by Rybicki & Hummer (1983), and here this is the same as CM96’s equation 8, where $\tilde{\nu} = \nu_0 (1 + \frac{v_l}{c})$ is the Doppler-shifted resonant frequency of the line as seen by the observer, i.e. $v_l = \sin i (v_r \cos \phi - v \phi \sin \phi) = -\sin i v \phi \sin \phi$. Note that this is only the classical Doppler shift from circular motion, and does not include the effects of relativity or transverse motion. Any effect from transverse motion would act uniformly on our disk and would only shift the center of the line profile, but the relativistic redshift is radially dependent and should be of order $1.5(r_s/r) \times 10^5 \text{ km/s}$ (Waters et al. 2016). Fortunately the characteristic size of the BLR is of order $10^3 r_s$ and thus we do not model this effect as it is not significant over the width of the line profile. Here k is the integrated line opacity, β the escape probability, and S the source function. This relationship is essentially the familiar equation for the formation of a spectral line, but the usual line function $\phi(x)$ is replaced with the Dirac-delta function in keeping with the Sobolev approximation.

If we also consider continuum variability, there will be an associated time lag at each disk location in addition to the Doppler shift. Adding this in gives us the so-called “transfer function” (as shown in Waters et al. (2016)):

$$\Psi(t, \nu) = \iint r k(r) \beta(r, \phi, i) S(r) \delta[\nu - \tilde{\nu}(\phi, r)] \delta[t - \tilde{t}] dr d\phi \quad (3)$$

The line profile is then just $\int_0^\infty \Psi(t, \nu) dt$ and the so-called response function is $\int_{-\infty}^\infty \Psi(t, \nu) d\nu$, which we illustrate with echo images of our best fit in the results section.

In the Sobolev approximation we can express the escape probability as $\beta = \frac{1-e^{-\tau}}{\tau}$, and in the limit where the velocity gradients are large (and thus the Sobolev optical depth is very high) we have simply $\beta \approx \frac{1}{\tau} = \left(\frac{\nu_0}{k(r)c} \right) \left| \frac{dv_l}{dt} \right|$. Thus we can express the quantity $k(r)\beta(r) = \frac{\nu_0}{c} \left| \frac{dv_l}{dt} \right|$.

As discussed in Waters et al. (2016) (hereafter Waters16), it is common to adopt a power-law dependence for source function, i.e. $S(r) = A(r)F_X^{\eta(r)}$, where F_X is the flux from the continuum and the power law index $\eta(r) = \frac{\partial \ln S_l}{\partial \ln F_X}$ (Krolik et al. 1991). Typical η values from photoionization modeling are between 0 and 2, and to match previous work done in Waters16 and CM96 we choose a constant value of $\eta = 1$. We also assume that the flux from the continuum originates from a region much closer to the black hole than the BLR (as is the premise of the reverberation mapping technique) and is emitted spherically and isotropically such that the flux scales like $F_X \propto \frac{1}{r^2}$ in its interaction with the BLR. For $A(r)$ we adopt the prescription $A(r) = A_0 r^\gamma$, and we choose $\gamma = 1$ to match with CM96. Overall this makes $S(r) \propto \frac{1}{r}$ and thus equation 3 (with all of our prescriptions applied) is just:

$$\Psi(\nu) = \frac{A_0 \nu_0}{4\pi c} \int_{r_{\min}}^{r_{\max}} \int_0^{2\pi} \left| \frac{dv_l}{dt} \right| \delta[\nu - \tilde{\nu}] dr d\phi \int_0^\infty \delta[t - \tilde{t}] dt \quad (4)$$

We will evaluate this integral numerically with the following general approach:

1. First, we make a 2D disk in log polar coordinates, where each cell has coordinates (r, ϕ) that correspond to an associated resonant Doppler shift $\tilde{\nu}$ and time delay \tilde{t} .
2. We then calculate the weighted intensity at each location within the disk as given by 4.
3. Finally, we integrate to get the total line luminosity, binning the disk according to $\tilde{\nu}$ and summing over all time delays to get the line profile and vice versa to obtain the response function. This ensures each region of the disk only contributes to the total intensity integral at its corresponding resonant Doppler frequency as is required by the Dirac-delta function in equations 2-4.

We must now evaluate $\left| \frac{dv_l}{dt} \right|$. The line of sight velocity gradient can be found using the rate of strain tensor $\hat{n} \cdot \mathbf{A} \cdot \hat{n}$ (often denoted as $Q = \sum_{i,j} \frac{1}{2} \left(\frac{\partial v_i}{\partial r_j} + \frac{\partial v_j}{\partial r_i} \right)$)—shears in the disk create the velocity gradients we seek to recover, which we will now derive. The \hat{n} for this geometry at an observer of $\phi = 0$ and inclination i is given by Waters16 as:

$$\begin{aligned} \hat{n} = & (\sin \theta \cos \theta \sin i + \cos \theta \cos i) \hat{r} \\ & + (\cos \theta \cos \phi \sin i - \sin \theta \cos i) \hat{\theta} \\ & - (\sin \phi \sin i) \hat{\phi} \end{aligned} \quad (5)$$

Using this \hat{n} and the rate of strain tensor terms in spherical coordinates from Batchelor (1968) we can write the line of sight velocity gradient as:

$$\begin{aligned} \hat{n} \cdot \mathbf{A} \cdot \hat{n} = & \sin^2 i \left[\frac{\partial v_r}{\partial r} \cos^2 \phi - \left(\frac{\partial v_\phi}{\partial r} - \frac{v_\phi}{r} \right) \sin \phi \cos \phi \right. \\ & \left. + \frac{v_r}{r} \sin^2 \phi \right] \\ & - \sin i \cos i \left[\left(\frac{1}{r} \frac{\partial v_r}{\partial \theta} + \frac{\partial v_\theta}{\partial r} - \frac{v_\theta}{r} \right) \cos \phi \right. \\ & \left. - \frac{1}{r} \frac{\partial v_\phi}{\partial \theta} \sin \phi \right] \\ & + \cos^2 i \left(\frac{1}{r} \frac{\partial v_\theta}{\partial \theta} + \frac{v_r}{r} \right) \end{aligned} \quad (6)$$

Where in arriving at the form above we have assumed all of the $\frac{\partial}{\partial \phi}$ operator terms are 0 (axisymmetric) and the disk is in the equatorial plane ($\theta = \frac{\pi}{2}$) which allows us to significantly simplify the result. A more thorough derivation of equation 6 is given in the appendix. CM96 immediately discarded the θ terms, but we keep them here to generalize the wind in both the “vertical” and radial directions. Waters16 uses a ϕ convention for the observer that differs from CM96 by $-\frac{\pi}{2}$, but we can easily recover the result in CM96 by applying this shift:

$$\begin{aligned} \hat{n} \cdot \mathbf{A} \cdot \hat{n} = & \sin^2 i \left[\frac{\partial v_r}{\partial r} \sin^2 \phi + \left(\frac{\partial v_\phi}{\partial r} - \frac{v_\phi}{r} \right) \sin \phi \cos \phi \right. \\ & \left. + \frac{v_r}{r} \cos^2 \phi \right] \\ & - \sin i \cos i \left[\left(\frac{1}{r} \frac{\partial v_r}{\partial \theta} + \frac{\partial v_\theta}{\partial r} - \frac{v_\theta}{r} \right) \sin \phi \right. \\ & \left. + \frac{1}{r} \frac{\partial v_\phi}{\partial \theta} \cos \phi \right] \\ & + \cos^2 i \left(\frac{1}{r} \frac{\partial v_\theta}{\partial \theta} + \frac{v_r}{r} \right) \end{aligned} \quad (7)$$

For the rest of this work we will use the ϕ convention specified in Waters16 (equation 6).

In CM96 they assume that $v_r \approx 0$ (thin-disk model) but that there is an acceleration related to the escape velocity, ie $\frac{\partial v_r}{\partial r} \approx 3\sqrt{2}\frac{v_\phi}{r}$, where $v_\phi = \sqrt{\frac{GM}{r}}$ is the Keplerian v_ϕ , which gives us $\frac{\partial v_\phi}{\partial r} = \frac{-v_\phi}{2r}$. These accelerations are important, as in Sobolev theory the velocity gradients essentially give us the escape probability of photons resonating in the optically thick medium of the disk, and it is these escaping photons that we image (Sobolev 1957; Rybicki & Hummer 1983).

But what are the θ terms? Following in the footsteps of CM96 it makes sense to assume that on average $v_\theta \approx 0$ for the same reason $v_r \approx 0$, but similarly we will assume a particle may be lifted by the wind and accelerated to the local escape velocity (but now in the $\hat{\theta}$ direction) such that $\frac{\partial v_\theta}{\partial \theta} \approx \frac{v_{esc}}{(H/R)}$ and $\frac{\partial v_\theta}{\partial r} \approx \frac{\partial v_r}{\partial r}$. Since $v_\phi(r) \rightarrow \frac{\partial v_\phi}{\partial v_\theta} = 0$, and we also set $\frac{\partial v_r}{\partial \theta} = 0$ in keeping with the idea of a thin disk.

Plugging in these approximations reduces equation 7 to:

$$\begin{aligned} \hat{n} \cdot \mathbf{A} \cdot \hat{n} = & 3\frac{v_\phi}{r} \sin^2 i \cos \phi \left[\sqrt{2} \cos \phi + \frac{\sin \phi}{2} \right] \\ & - \sin i \cos i \left[3\sqrt{2}\frac{v_\phi}{r} \cos \phi \right] \\ & + \cos^2 i \left(\frac{1}{r} \frac{v_{esc}}{(H/R)} \right) \end{aligned} \quad (8)$$

Rescaling v_ϕ into units of r_s gives us $v_\phi = \sqrt{\frac{1}{2r'}}$ and $v_{esc} = \sqrt{\frac{1}{r'}}$ (where $r' = r/r_s$, so $r = r'r_s$), which, after simplifying, gives us:

$$\begin{aligned} \hat{n} \cdot \mathbf{A} \cdot \hat{n} = & \frac{c^3}{2GM} \sqrt{\frac{1}{2r'^3}} \left[3 \sin^2 i \cos \phi \left(\sqrt{2} \cos \phi + \frac{\sin \phi}{2} \right) \right. \\ & \left. - 3\sqrt{2} \sin i \cos i \cos \phi + \frac{\sqrt{2}}{(H/R)} \cos^2 i \right] \end{aligned} \quad (9)$$

Qualitatively we can break the terms down as follows:

1. The first term largely describes radial shear from the wind, where the angular dependence allows photons with small Doppler shifts to escape more easily to the observer from regions with large radial shears at the near and far sides of the disk ($\phi \approx 0, \pi$, where the line of sight projected velocities are small).
2. The second term describes gradients caused by Keplerian shear in the disk, which by itself produces a

double-peaked line profile (with peaks corresponding to the blue and red sides of the disk), replicating the “M profile” first shown in Rybicki & Hummer (1983).

3. The third term represents the “lifting” shear as a function of radius, where again the angular dependence allows photons with small Doppler shifts to escape more easily (although less strongly than in the case of radial shear).
4. The final term represents the “lifting” shear as a function of height off of the disk, and it interestingly has no angular dependence, meaning it represents a form of isotropic emission that by itself produces a doubly peaked line profile, albeit of a different shape than the profile given by just the Keplerian shear. For thin disks $H \ll R$ and thus even a small velocity gradient in the θ direction will be amplified greatly by this term.

This is the crux of our model, as the emission intensity at each location in the disk is then given by:

$$I(r) = \frac{\nu_0}{4\pi r^2 c} A(r) \left| \frac{dv_l}{dl} \right| (1 - e^{-\tau_\nu}) \quad (10)$$

with $A(r) = A_0 r^\gamma$. Here we choose $\gamma = 1$ to match with the analytic solution considered by CM96.

To better explore the parameter space we want to examine how each of these terms affect the line profile shape. When the velocity gradients are large $\tau \gg 1$ and thus 10 becomes directly proportional to the line of sight velocity gradient. This makes it the critical component that shapes the line and response profiles. Discarding the normalization and primes, we can explore how this line of sight velocity gradient changes as a function of r , i , and ϕ alone:

$$\begin{aligned} \hat{n} \cdot \mathbf{A} \cdot \hat{n} \approx \frac{dv_l}{dl} \approx & \sqrt{\frac{1}{2r'^3}} \left(3 \sin^2 i \cos \phi \left[\sqrt{2} f_1 \cos \phi + f_2 \frac{\sin \phi}{2} \right] \right. \\ & \left. - 3 f_3 \sin i \cos i \cos \phi + \sqrt{2} f_4 \cos^2 i \right) \end{aligned} \quad (11)$$

Neglecting physical constants, this completes the mathematical description of our model, where $f_{1,2,3,4}$ are constants that allow us to artificially vary the strength of the different wind launching terms described above. In the high inclination limit only the $\sin^2 i$ term is important and our result reduces to the form considered in CM96, however at low inclinations the $\cos^2 i$ term is very important (which was not previously explored), and the

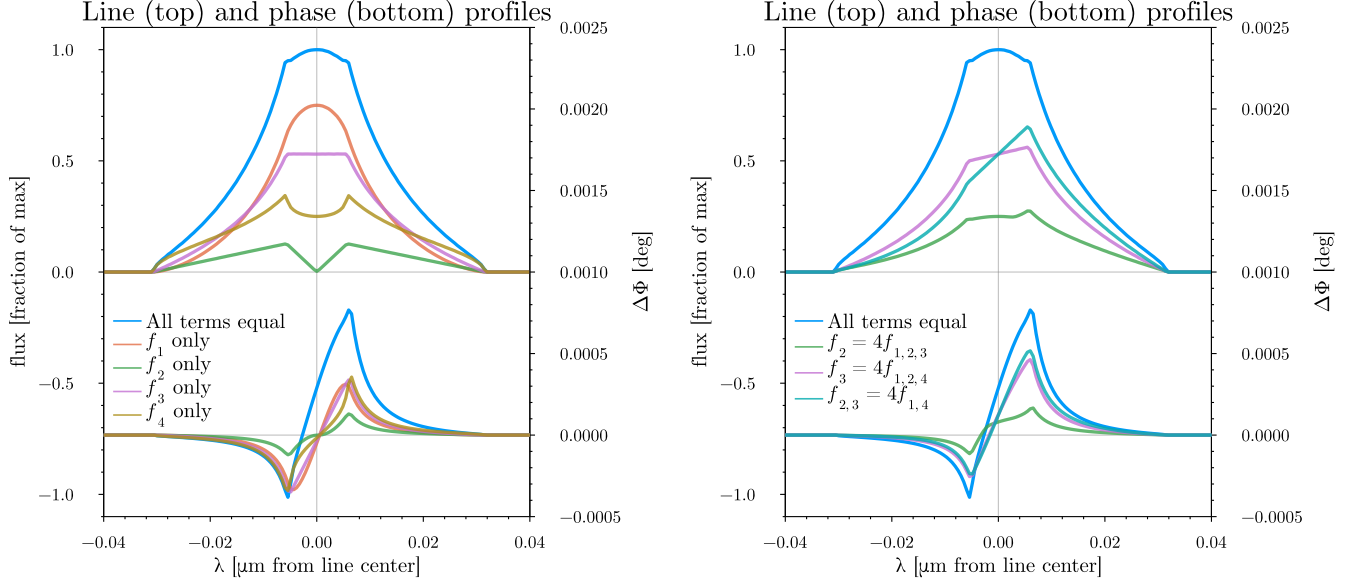


Figure 2. Left panel: Comparison of the different terms and their resulting line and phase profiles. Here the models all share the following parameters that can also influence the shape of the profiles: $i = 45^\circ$, $\bar{r} = 3000r_s$, $M_{\text{BH}} = 3 \times 10^8 M_\odot$, $r_{\text{min}} =$, $r_{\text{max}} =$, and $\theta_{\text{rot}} = 330^\circ$ —the most important/obvious of which are the rotation angle and the inclination. These parameters were chosen arbitrarily to be simple, representative values—the takeaway from this plot is the importance of the difference terms to the shape of the line/phase profile as described in the text. The influence of these parameters on the shape of the line profile is further discussed in the text below.

Right panel: Similar to the left panel, only this time we show only the total model lines but with varying ratios of f_2 and f_3 , better illustrating their qualitative effects on the line/phase profiles as described in the text. The blue profile plotted here (where all terms have equal weights) matches the blue profile plotted in the left panel, and all other model parameters are the same as those used in creating the left panel.

addition of both terms at moderate inclinations make a significant difference when compared with the results shown in CM96. It is also important to note here that we have absorbed the constant H/R into f_4 .

Figure 2 explores the general behavior of these terms and how they affect the shape of the line and phase profiles. Qualitatively, the terms have the following effects on the line profile:

1. f_1 creates a symmetric bell-curve like shape about the line center, as it is proportional to $\cos^2 \phi$.
2. f_2 in isolation creates an “M” shaped line profile with two peaks, with the line center as a minimum. This replicates the result first shown in RH83’s figure 2. In conjunction with other terms it acts to depress the region just to the left of the center of the line profile, and to raise the region just to the right of the center as it is proportional to $\cos \phi \sin \phi$, providing a left/right asymmetry to the line profile.
3. f_3 in isolation creates a “plateau” shaped line profile, with the “plateau” feature centered on the line center, but in conjunction with other terms it acts to widen the line profile and alter the shape of the

peak, as it is proportional to $\cos \phi$ and in our definition the observer is at $\phi = 0$, meaning there is no left/right asymmetry.

4. f_4 creates a symmetric “twin horns” type feature, as it is an isotropic emission feature and thus only depends on the Doppler shift, i.e. the frequency shift is proportional only to $\sqrt{\frac{1}{2r}} \sin i \cos \phi$. This is analogous to the dash-dot profile shown in CM96’s figure 2. Its shape is thus entirely dependent on the delta function Doppler resonance—gas on the bluer/redder sides of the disk resonates in blue/red wavelengths and thus only contributes on the corresponding side of the line profile, while the gas with no Doppler shift close to the front and back sides of the disk keeps the line profile from going to zero at line center.

Regardless of whether the individual term would produce a single or double peaked line profile, all of the phase profiles display the standard “S” shape, but with different morphologies. As shown in figure 2, when all the terms are of equal strength f_1 and f_4 dominate.

Our code uses this model prescription to generate a two-dimensional ray-traced image of an inclined disk

assumed to represent the BLR, employing a polar coordinate grid with logarithmic radial spacing. The intensity at each grid cell in the disk is given by equations 10 and 11, and we can calculate the line profile numerically as described above (with the summed intensities at each disk location weighted by their corresponding area element). In fitting we allow the terms to vary as $0 \leq f_{1,2,3,4} \leq 1$ consistent with the disk launching outflows. The differential phase is calculated following the standard BLR photocenter and kinematic modelling prescription in the marginally resolved limit, where we keep only the first order term in the expansion of the complex visibility such that $\Delta\phi = -2\pi(u \cdot \bar{x}) \frac{f}{1+f}$ (Lachaume (2003), Waisberg et al. (2017)). Here u are the interferometric baselines, \bar{x} the on-sky emission centroids, and f the normalized line flux such that $\frac{f}{1+f}$ represents the contrast between the line and the continuum. Note that this $\Delta\phi$ does not refer to any physical ϕ in the disk and is only the differential phase angle.

We use data previously published by the GRAVITY collaboration on Quasar 3C 273 to fit our model—for a detailed description of the observations and reduction techniques used see GRAVITY Collaboration et al. (2019). 3C 273 is uniquely suited to test the model because the system’s distance is close enough that the broad-line region can be marginally spatially resolved by GRAVITY but also oriented such that we observe the jet, allowing us to constrain the what we believe the “true” inclination of the system to be (Kundt & Gopal-Krishna 1986). The fitting is done with flux and phase measurements along each wavelength channel (measurements taken in 40 channels between ~ 2.13 and $\sim 2.22 \mu\text{m}$ over six baselines at four different epochs), using Monte Carlo methods. To ensure we sample a large region of the parameter space we employ a parallel tempered Monte Carlo method developed by Voudsen et al. (2016); Foreman-Mackey et al. (2013), using six different logarithmically spaced temperatures each with 24 walkers. The model as we fit to the data is fully described by the following 11 parameters:

1. The inclination angle of the system i , where $i = 90^\circ$ corresponds to an edge-on viewing angle and $i = 0^\circ$ a “face-down” viewing angle as shown in 1. Higher values of i lead the first term in equation 6 to be the dominant drivers of the line and phase profiles, with lower values leading the last term to be most significant.
2. The mass of the central supermassive black hole, M_{BH} . Increasing the mass of the black hole increases the amplitude of the phase profile.

3. The mean radius of the BLR as weighted by the intensity of emission $I(r)$:

$$\bar{r} = \frac{\int_{r_{\min}}^{r_{\max}} r I(r) dr}{\int_{r_{\min}}^{r_{\max}} I(r) dr} = \left(\frac{r_{\max}^{\gamma-3/2} - r_{\min}^{\gamma-3/2}}{r_{\max}^{\gamma-5/2} - r_{\min}^{\gamma-5/2}} \right) \left(\frac{\gamma-5/2}{\gamma-3/2} \right)$$

Higher values of \bar{r} lead to the line/phase profiles being “squished” in λ space.

4. A size scaling factor r_{fac} , which in conjunction with \bar{r} gives the minimum and maximum radii of the BLR via $r_{\min} = \bar{r} \left(\frac{r_{\text{fac}}^{\gamma-5/2} - 1}{r_{\text{fac}}^{\gamma-3/2} - 1} \right) \left(\frac{\gamma-3/2}{\gamma-5/2} \right)$ and $r_{\max} = r_{\text{fac}} r_{\min}$. In keeping with CM96 we fix γ to be 1 in this work. Increasing r_{fac} slightly “stretches” the line/phase profiles in λ space, and also steepens the slope in the S-curve of the phase profile connecting the negative and positive peaks. This also increases the total flux of the line, but this doesn’t affect the fit as we are only seeking to match the characteristic line shapes.
5. The proportional strength of the radial shear wind term, f_1 .
6. The proportional strength of the Keplerian shear term, f_2 .
7. The proportional strength of the radial lifting shear term, f_3 .
8. The proportional strength of the height lifting shear term, f_4 .
9. The rotation of the model with respect to the orientation of the baselines in the data. We report the results in term of the standard position angle convention, but the model itself is fit with a convention that is 90 degrees offset from this.
10. A parameter that can vary the normalization of the line profile with respect to the data slightly as the data points may not be exactly at the peak of the line, $n \geq 1$, where $n = 1$ corresponds to scaling the model exactly to the maximum flux measurement in the data.
11. A parameter that varies the line center, thus slightly shifting the models left and right in λ space. Here we model Pa α line emission, which has a known center near $\lambda_c \approx 2.172 \mu\text{m}$ for 3C273 at a redshift of ~ 0.16 .

Table 1. MCMC fit parameters

i	M_{BH}	\bar{r}	r_{fac}	f_1	f_2	f_3	f_4	θ_{PA}	n	λ_c
(1)	(2)	(3)	(4)	(5)	(6)	(7)	(8)	(9)	(10)	(11)
$75^{+8.8^\circ}_{-11}$	$7.8^{+0.15}_{-0.11} \times 10^7 M_\odot$	$6200^{+580}_{-800} r_s$	$45^{+6.0}_{-4.9}$	$0.57^{+0.25}_{-0.21}$	$0.65^{+0.25}_{-0.38}$	$0.47^{+0.35}_{-0.33}$	$0.25^{+0.42}_{-0.21}$	$240^{+6.8^\circ}_{-5.2}$	$1.0^{+0.009}_{-0.004}$	$0.00025^{+0.0}_{-0.0} \mu\text{m}$

NOTE—Means with 50th percentile confidence intervals (to two significant figures) on each of our 11 fit parameters. f_3 and f_4 are particularly poorly constrained, a result of the higher inclination preference of the sampler.

3. RESULTS

After fitting the model as described in the previous section, we reached convergence after $\sim 10,000$ iterations in each walker at each temperature. We consider the fit converged when the maximum autocorrelation time of any parameter is 1% of the total number of steps taken. We show only the lowest temperature in our results presented below as the upper temperatures are designed to explore the parameter space and “trickle” down to the lowest temperature for further refinement (Vousden et al. 2016). Most importantly, the fit generally prefers higher inclinations and lower black hole mass. Table 1 presents the mean values in the fit with 50% confidence intervals.

Figure 3 shows our best fit to the line and phase profiles, and table 1 shows our average fit parameters from the result of our parallel tempered MCMC run as described in the methods section. The appendix shows a corner plot (8) of all of our parameters with their associated one-dimensional histograms. The fit is good, with a reduced χ^2 value of ~ 1.36 for the mean parameters (and ~ 1.35 for the best fit). The fit prefers higher inclinations, leading to only the $f_{1,2}$ terms being significant in the fit. The uncertainty on the importance of the wind terms with respect to each other is large and thus it is difficult to draw conclusions on the importance of any aspect over another, aside from the larger importance in $f_{1,2}$ that is largely driven by the inclination dependence. This appears to match observational evidence that there they be a large radial component of any disk-wind outflows (Vestergaard et al. 2000).

The black hole mass and on-sky position angle are the physical parameters best constrained by our model. Using the mean mass value and taking the distance to 3C 273 as ~ 550 Mly (as done in GRAVITY Collaboration et al. (2019)) the inferred BLR size is of order $\sim 20 \mu\text{as}$. Assuming this same distance and the observed luminosity of 3C 273 our mean black hole mass implies that the system is super-Eddington by a factor of a few (Greenstein & Schmidt 1964). Figure 4 shows how our model centroids compare to those in the data, in good agreement with ordered rotation around the jet.

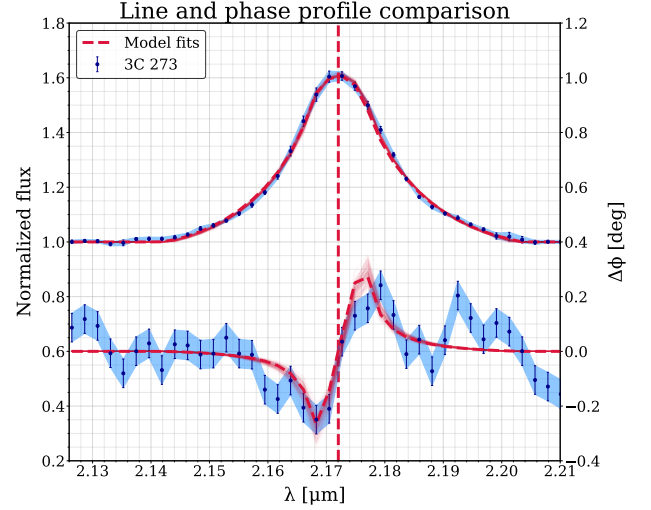


Figure 3. The resulting line/phase profiles from our best fit. The full parameter list is contained in table 1. The dashed red line is the best fit from the model, while the translucent red lines are 100 random draws from the sampler showcasing the spread of the fit. The line profile is significantly better fit than the phase profile, which is much noisier. The phase profile shown here is an average of the phases recovered from the baselines which are significantly misaligned with the jet. We show the same baselines here as in GRAVITY Collaboration et al. (2019)—figures 6 and 7 in our appendix show all of the individual phase profiles and the uv coverage of the observations, illustrating why this choice is made.

4. DISCUSSION

In comparing with the cloud model fit previously published by the GRAVITY collaboration the only physical system parameter the models \sim agree on is the position angle. If the disk-wind model correctly described the BLR physics our model would predict a black hole mass lower by a factor of ~ 5 compared with results previously published in GRAVITY Collaboration et al. (2019), while implying an angular size of the broad-line region that is smaller by a factor of ~ 2 . The reduced χ^2 presented for the cloud model fit in GRAVITY Collaboration et al. (2019) is given as ~ 1.3 , which to two significant figures is slightly better than our reduced

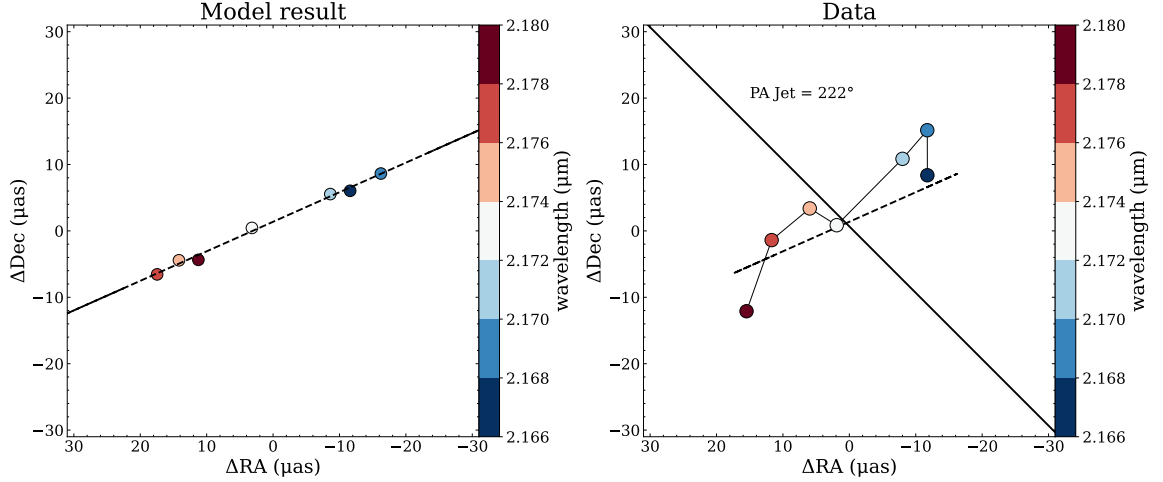


Figure 4. Centroids from our model sampled at the same wavelengths in the data are shown in the left panel, with a best fit line representing the centroid track. The right panel shows the data centroids with the solid black line representing the PA of the jet as shown in [GRAVITY Collaboration et al. \(2019\)](#) and the dashed black line corresponding to the model centroid track as shown in the left panel. An interesting comparison to note here is that the $\bar{r} \approx 17\mu\text{as}$ in our fit essentially matches the extent of the data centroids shown as our model is a disk governed by Keplerian rotation, while the result in [GRAVITY Collaboration et al. \(2019\)](#) corresponds to a significantly larger mean size for the BLR of $\sim 50\mu\text{as}$, illustrating that the emission centroids showing ordered rotation significantly underestimate the true size of the BLR in the cloud model.

$\chi^2 \sim 1.35$. Still, both models appear to fit the data with roughly the same quality, and this implies possible systematic errors in estimating both the size of the BLR and the mass of the central black hole from interferometry data by factors of ~ 2 and ~ 5 respectively.

While both models appear to fit the data well, observations indicate that the true inclination angle of 3C 273 is $\sim 20 \pm 10^\circ$ ([Kundt & Gopal-Krishna 1986](#)). This disfavors the disk-wind model presented here, and implies the cloud model is a better explanation for the physics of the underlying broad-line region, but we do not rule out the disk-wind model completely, especially for other AGN. Our model is simple, including only four possible wind launching terms simplified under the Sobolev approximation to rely on strong velocity gradients motivated by the local escape speed in the optically thick regime. It may be possible that extending the model further (either by adding more terms and/or discarding some of the idealizations considered here, such as axisymmetry and the ideal 2D thin-disk) could result in different best fit values—which could bring the inclination of the fit more in alignment with the current observational constraints—but in doing so the complexity of the model would increase dramatically. Any model of sufficient complexity can adequately fit any dataset, but as the model increases in complexity the amount of knowledge and intuition gained about the system correspondingly often decreases, which is part of the reason we limited our exploration of the terms to only those we felt were

easiest to justify physically and thus feel that the result here is (barring some drastic change in the inferred true value of the inclination angle) unphysical, lending further support to the cloud model. The cloud model also favors a higher black hole mass, which in their fit makes the luminosity \sim the Eddington luminosity (instead of super-Eddington).

We also calculate an echo image of our best fit (shown in figure 5), to compare to reverberation mapping techniques and illustrate a mapping of the resonance conditions within our disk that produce the line and response profiles. As shown in Waters16, for a thin disk under Keplerian rotation the resonance condition in frequency space is simply given by the Doppler shift $\tilde{\nu} = \nu_0(1 - \sin\phi \sin i)$, while the resonance condition for the time delay $t = \frac{r}{c}(1 - \cos\phi \sin i)$. Here we plot the change in frequency $\Delta\nu$ in units of Mm/s, i.e. $\Delta\nu = c\Delta\nu = -v_\phi \sin\phi \sin i$. The weighted mean (using Ψ) time lag from our solution is ~ 160 days (using our mean black hole mass), and the mean light travel time to our best fit value for \bar{r}_{BLR} is ~ 200 days, with the light travel time to our r_{\min} being ~ 82 days. The most recent results published by [Zhang et al. \(2019\)](#) have measured time delays of $\sim 145 \pm 10$ days in the rest frame of 3C273 using the $H\beta$ and $H\gamma$, while older results favor longer time delays of ~ 300 days ([Kaspi et al. \(2000\)](#), [Peterson et al. \(2004\)](#)). Our results for both the weighted average and time delay and mean time delay associated with our \bar{r} are between these extremes.

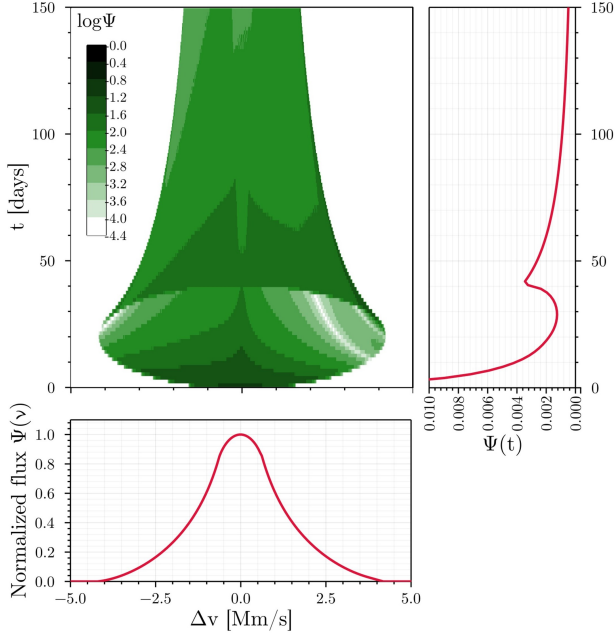


Figure 5. An echo image of our model solution. In comparing to the figures in the appendix of Waters16 or figures 2, 4, and 5 in CM96 we see many similarities, but there are minor differences that come from us considering additional terms in our fit (for example, the region on the right at low t of our plot). The mean time lag (defined as $\langle t \rangle = \frac{\int_0^\infty t\Psi(t)dt}{\int_0^\infty \Psi(t)dt}$) is ~ 160 days. Our best fit to \bar{r}_{BLR} corresponds to a time delay of ~ 200 days (roughly $1/3$ the value for the \bar{r} found in GRAVITY Collaboration et al. (2019)), our value of r_{\min} corresponds to a time delay of ~ 80 days, and our value for r_{\max} corresponds to a time delay of ~ 10 years.

The previously published result in GRAVITY Collaboration et al. (2019) produced a characteristic time delay of $\sim 145 \pm 35$ days at their value of r_{\min} (corresponding to $\sim 11\mu\text{as}$ on the sky), while the characteristic time delay at their \bar{r} is ~ 600 days—significantly longer than ours as the scales our model produces are roughly twice as small. While we model $P\alpha$, Sellgren et al. (1983) have shown that the line profiles between $H\beta$, $H\gamma$, and $P\alpha$ are all broadened similarly, indicating they are likely all originating from the same broad-line region and thus the comparison is appropriate.

5. CONCLUSIONS

We have fit a simple disk-wind launching model to GRAVITY data, showing that such a model can fit the line profiles, phase profiles, and emission centroids observed by GRAVITY as well as match the expected order of magnitude for time delays in response to a variable continuum. Our fit results in a smaller black hole mass for 3C 273 ($\approx 8 \times 10^7 M_\odot$) than other modelling results, which would make the system likely super Edding-

ton given its observed luminosity (Greenstein & Schmidt 1964). If our model were an accurate depiction of the true physics and geometry of the broad-line region we would expect all supermassive black hole measurements that rely on the widths of broad-line profiles to be overestimates by a factor of a few (see 1).

However, in order to create a single peak in the line profile our fit requires the inclination of the model system to be much higher than what is inferred for 3C 273 from observations of the jet. Our fit prefers an inclination angle of $\sim 75^\circ$, while the jet for 3C 273 indicates an inclination angle of $\sim 20 \pm 10^\circ$ (Kundt & Gopal-Krishna 1986). Assuming the jet and the disk are not significantly misaligned, the cloud model presented by GRAVITY Collaboration et al. (2019) appears to thus be a better potential explanation of the underlying physics and geometry governing the broad-line region, as the phase and line profile fits in that work are at least as good as in our model but the cloud model produces a fit at much lower inclinations ($\sim 12^\circ$) as expected given the observational constraints on the jet orientation of 3C 273.

Our model is simple and there may be extensions that further improve the fit we have not considered in this work. Furthermore it may be possible that not all quasar BLRs are governed by the same physics, and while 3C 273 may not be governed by disk-wind launching dynamics other quasars may still be. We hope to extend this work to other objects as a final test case, but believe that this initial result provides strong support for the cloud model. If the evidence continues to favor the cloud model (as this result does) it is of increasing importance to try to better understand the physical processes that can result in a distribution of cold and dense puffed up clouds of atomic gas surrounding AGN, as well as how this picture can be connected to the strong observational evidence for outflows.

6. ACKNOWLEDGMENTS

This work was supported in part by NSF grant AST-1909711 and an Alfred P. Sloan Research Fellowship (JD). We are grateful to the computing resources made available to us by Research Computing at CU Boulder, as this work utilized the Summit supercomputer, which is supported by the National Science Foundation (awards ACI-1532235 and ACI-1532236), the University of Colorado Boulder, and Colorado State University. The Summit supercomputer is a joint effort of the University of Colorado Boulder and Colorado State University. Kirk is especially grateful to his office-mate Sajal Gupta for many helpful discussions over the course of the project, and to Marcel Corchado-Abelo for discus-

sions on the rate of strain tensor. Finally, Kirk would like to thank his family and friends for their support

in his Ph.D. journey and in celebrating this first paper milestone.

Facilities: VLTI(GRAVITY)(GRAVITY Collaboration et al. 2017)

Software: Julia, ptemcee, python

REFERENCES

- Batchelor, G. 1968, Quarterly Journal of the Royal Meteorological Society, 94, 435, doi: [10.1002/qj.49709440128](https://doi.org/10.1002/qj.49709440128)
- Bottorff, M. C., Korista, K. T., Shlosman, I., & Blandford, R. D. 1997, in Astrophysics and Space Science Library, Vol. 218, Astronomical Time Series, ed. D. Maoz, A. Sternberg, & E. M. Leibowitz, 247, doi: [10.1007/978-94-015-8941-3_35](https://doi.org/10.1007/978-94-015-8941-3_35)
- Chiang, J., & Murray, N. 1996, ApJ, 466, 704, doi: [10.1086/177543](https://doi.org/10.1086/177543)
- Elvis, M. 2000, ApJ, 545, 63, doi: [10.1086/317778](https://doi.org/10.1086/317778)
- Foreman-Mackey, D. 2016, The Journal of Open Source Software, 1, 24, doi: [10.21105/joss.00024](https://doi.org/10.21105/joss.00024)
- Foreman-Mackey, D., Hogg, D. W., Lang, D., & Goodman, J. 2013, PASP, 125, 306, doi: [10.1086/670067](https://doi.org/10.1086/670067)
- GRAVITY Collaboration, Abuter, R., Accardo, M., et al. 2017, A&A, 602, A94, doi: [10.1051/0004-6361/201730838](https://doi.org/10.1051/0004-6361/201730838)
- . 2019, The Messenger, 178, 20, doi: [10.18727/0722-6691/5166](https://doi.org/10.18727/0722-6691/5166)
- Greenstein, J. L., & Schmidt, M. 1964, ApJ, 140, 1, doi: [10.1086/147889](https://doi.org/10.1086/147889)
- Hamann, F., Korista, K. T., & Morris, S. L. 1993, ApJ, 415, 541, doi: [10.1086/173185](https://doi.org/10.1086/173185)
- Kaspi, S., Smith, P. S., Netzer, H., et al. 2000, ApJ, 533, 631, doi: [10.1086/308704](https://doi.org/10.1086/308704)
- Krolik, J. H., Horne, K., Kallman, T. R., et al. 1991, ApJ, 371, 541, doi: [10.1086/169918](https://doi.org/10.1086/169918)
- Kundt, W., & Gopal-Krishna. 1986, Journal of Astrophysics and Astronomy, 7, 225, doi: [10.1007/BF02714211](https://doi.org/10.1007/BF02714211)
- Lachaume, R. 2003, A&A, 400, 795, doi: [10.1051/0004-6361:20030072](https://doi.org/10.1051/0004-6361:20030072)
- Lynden-Bell, D. 1969, Nature, 223, 690, doi: [10.1038/223690a0](https://doi.org/10.1038/223690a0)
- Peterson, B. 2006, in Physics of Active Galactic Nuclei at all Scales, ed. D. Alloin, R. Johnson, & P. Lira (Berlin, Heidelberg: Springer Berlin Heidelberg), 77–100, doi: [10.1007/3-540-34621-X_3](https://doi.org/10.1007/3-540-34621-X_3)
- Peterson, B. M., Ferrarese, L., Gilbert, K. M., et al. 2004, ApJ, 613, 682, doi: [10.1086/423269](https://doi.org/10.1086/423269)
- Rees, M. J. 1984, ARA&A, 22, 471, doi: [10.1146/annurev.aa.22.090184.002351](https://doi.org/10.1146/annurev.aa.22.090184.002351)
- Rybicki, G. B., & Hummer, D. G. 1983, ApJ, 274, 380, doi: [10.1086/161454](https://doi.org/10.1086/161454)
- Sagiv, I., Gal-Yam, A., Ofek, E., et al. 2014, The Astronomical Journal, 147, 79, doi: [10.1088/0004-6256/147/4/79](https://doi.org/10.1088/0004-6256/147/4/79)
- Sellgren, K., Soifer, B. T., Neugebauer, G., & Matthews, K. 1983, PASP, 95, 289, doi: [10.1086/131160](https://doi.org/10.1086/131160)
- Shakura, N. I., & Sunyaev, R. A. 1973, A&A, 24, 337
- Sobolev, V. V. 1957, Soviet Ast., 1, 678
- Vestergaard, M., Wilkes, B. J., & Barthel, P. D. 2000, ApJL, 538, L103, doi: [10.1086/312805](https://doi.org/10.1086/312805)
- Vousden, W. D., Farr, W. M., & Mandel, I. 2016, MNRAS, 455, 1919, doi: [10.1093/mnras/stv2422](https://doi.org/10.1093/mnras/stv2422)
- Waisberg, I., Dexter, J., Pfuhl, O., et al. 2017, ApJ, 844, 72, doi: [10.3847/1538-4357/aa79f1](https://doi.org/10.3847/1538-4357/aa79f1)
- Waters, T., Kashi, A., Proga, D., et al. 2016, ApJ, 827, 53, doi: [10.3847/0004-637X/827/1/53](https://doi.org/10.3847/0004-637X/827/1/53)
- Zhang, Z.-X., Du, P., Smith, P. S., et al. 2019, ApJ, 876, 49, doi: [10.3847/1538-4357/ab1099](https://doi.org/10.3847/1538-4357/ab1099)

APPENDIX

A. FULL DERIVATION OF THE LINE OF SIGHT VELOCITY GRADIENT

As discussed in the text, the line of sight velocity gradient $\frac{dv_l}{dl}$ can be approximated with the rate of strain tensor. In computing $\frac{dv_l}{dl} \approx \hat{n} \cdot \mathbf{\Lambda} \cdot \hat{n}$ as given in 6 we need the components of the rate of strain tensor Λ_{ij} in spherical geometry, which we obtain from Batchelor (1968). As in the text (see equation 5) we use:

$$\hat{n} = (\sin \theta \cos \phi \sin i + \cos \theta \cos i) \hat{r} + (\cos \theta \cos \phi \sin i - \sin \theta \cos i) \hat{\theta} - (\sin \phi \sin i) \hat{\phi} \quad (\text{A1})$$

Using this we evaluate $\hat{n} \cdot \mathbf{\Lambda} \cdot \hat{n}$ as:

$$\begin{aligned} \hat{n} \cdot \mathbf{\Lambda} \cdot \hat{n} = & \Lambda_{rr} (\sin \theta \cos \phi \sin i + \cos \theta \cos i)^2 + \Lambda_{\theta\theta} (\cos \theta \cos \phi \sin i - \sin \theta \cos i)^2 + \Lambda_{\phi\phi} (\sin \phi \sin i)^2 \\ & + 2\Lambda_{r\theta} (\sin \theta \cos \phi \sin i + \cos \theta \cos i) (\cos \theta \cos \phi \sin i - \sin \theta \cos i) \\ & - 2\Lambda_{\theta\phi} (\cos \theta \cos \phi \sin i - \sin \theta \cos i) (\sin \theta \sin i) - 2\Lambda_{r\phi} (\sin \theta \cos \phi \sin i + \cos \theta \cos i) (\sin \phi \sin i) \end{aligned} \quad (\text{A2})$$

Applying the approximation that the disk is very thin and at the midplane we set $\theta = \frac{\pi}{2}$, reducing equation A2 to:

$$\begin{aligned} \hat{n} \cdot \mathbf{\Lambda} \cdot \hat{n} = & \Lambda_{rr} (\sin \theta \cos \phi \sin i)^2 - \Lambda_{\theta\theta} (\sin \theta \cos i)^2 + \Lambda_{\phi\phi} (\sin \phi \sin i)^2 \\ & - 2\Lambda_{r\theta} (\sin \theta \cos \phi \sin i) (\sin \theta \cos i) \\ & + 2\Lambda_{\theta\phi} (\sin \theta \cos i) (\sin \theta \sin i) - 2\Lambda_{r\phi} (\sin \theta \cos \phi \sin i) (\sin \phi \sin i) \end{aligned} \quad (\text{A3})$$

Simplifying, this leaves us with:

$$\hat{n} \cdot \mathbf{\Lambda} \cdot \hat{n} = \sin^2 i (\Lambda_{rr} \cos^2 \phi + \Lambda_{\phi\phi} \sin^2 \phi - 2\Lambda_{r\phi} \sin \phi \cos \phi) - \sin i \cos i (2\Lambda_{r\theta} \cos \phi - 2\Lambda_{\theta\phi} \sin \phi) + \Lambda_{\theta\theta} \cos^2 i \quad (\text{A4})$$

From Batchelor (1968) the Λ_{ij} terms in spherical coordinates are:

$$\begin{aligned} \Lambda_{rr} = \frac{\partial v_r}{\partial r}; \Lambda_{\theta\theta} = \frac{1}{r} \frac{\partial v_\theta}{\partial \theta} + \frac{v_r}{r}; \Lambda_{\phi\phi} = \frac{1}{r \sin \theta} \frac{\partial v_\phi}{\partial \phi} + \frac{v_r}{r} + \frac{v_\theta \cot \theta}{r}; \\ \Lambda_{r\theta} = \frac{1}{2} \left(r \frac{\partial}{\partial r} \left(\frac{v_\phi}{r} \right) + \frac{1}{r} \frac{\partial v_r}{\partial \theta} \right); \Lambda_{\theta\phi} = \frac{1}{2} \left(\frac{\sin \theta}{r} \frac{\partial}{\partial \theta} \left(\frac{v_\phi}{\sin \theta} \right) + \frac{1}{r \sin \theta} \frac{\partial v_\theta}{\partial \phi} \right); \Lambda_{r\phi} = \frac{1}{2} \left(\frac{1}{r \sin \theta} \frac{\partial v_r}{\partial \phi} + r \frac{\partial}{\partial r} \left(\frac{v_\phi}{r} \right) \right) \end{aligned} \quad (\text{A5})$$

Here we again set $\theta = \frac{\pi}{2}$, and we also assume the disk is axisymmetric in ϕ such that all of the $\frac{\partial}{\partial \phi}$ terms are 0, reducing equation A5 to:

$$\begin{aligned} \Lambda_{rr} = \frac{\partial v_r}{\partial r}; \Lambda_{\theta\theta} = \frac{1}{r} \frac{\partial v_\theta}{\partial \theta} + \frac{v_r}{r}; \Lambda_{\phi\phi} = \frac{v_r}{r}; \\ \Lambda_{r\theta} = \frac{1}{2} \left(r \frac{\partial}{\partial r} \left(\frac{v_\phi}{r} \right) + \frac{1}{r} \frac{\partial v_r}{\partial \theta} \right); \Lambda_{\theta\phi} = \frac{1}{2} \left(\frac{\sin \theta}{r} \frac{\partial}{\partial \theta} \left(\frac{v_\phi}{\sin \theta} \right) \right); \Lambda_{r\phi} = \frac{1}{2} \left(r \frac{\partial}{\partial r} \left(\frac{v_\phi}{r} \right) \right) \end{aligned} \quad (\text{A6})$$

We now apply a final approximation to the disk, in which we assume that $v_r \approx v_\theta \approx 0$ in keeping with the standard assumptions for thin disks. Plugging this result into equation A4 then gives us:

$$\begin{aligned} \hat{n} \cdot \mathbf{\Lambda} \cdot \hat{n} = & \sin^2 i \left(\frac{\partial v_r}{\partial r} \cos^2 \phi - \left(r \frac{\partial}{\partial r} \left(\frac{v_\phi}{r} \right) \right) \sin \phi \cos \phi \right) \\ & - \sin i \cos i \left(\left(r \frac{\partial}{\partial r} \left(\frac{v_\phi}{r} \right) + \frac{1}{r} \frac{\partial v_r}{\partial \theta} \right) \cos \phi - \left(\frac{\sin \theta}{r} \frac{\partial}{\partial \theta} \left(\frac{v_\phi}{\sin \theta} \right) \right) \sin \phi \right) \\ & + \frac{1}{r} \frac{\partial v_\theta}{\partial \theta} \cos^2 i \end{aligned} \quad (\text{A7})$$

We now turn our attention to the derivatives. We assume Keplerian orbits such that $v_\phi = \sqrt{\frac{GM}{r}}$ and thus $\frac{\partial v_\phi}{\partial r} = \frac{-v_\phi}{2r}$. Applying this in conjunction with the chain rule, we can write: $r \frac{\partial}{\partial r} \left(\frac{v_\phi}{r} \right) = \frac{\partial v_\phi}{\partial r} - \frac{v_\phi}{r} = -\frac{3v_\phi}{2r}$. Similarly $r \frac{\partial}{\partial r} \left(\frac{v_\theta}{r} \right) =$

$\frac{\partial v_\theta}{\partial r} - \frac{v_\theta}{r}$ and $\frac{\sin \theta}{r} \frac{\partial}{\partial \theta} \left(\frac{v_\phi}{\sin \theta} \right) = \frac{1}{r} \frac{\partial v_\phi}{\partial \theta} - \frac{v_\phi}{r} \cot \theta = \frac{1}{r} \frac{\partial v_\phi}{\partial \theta}$. This reduces equation A7 to:

$$\begin{aligned} \hat{n} \cdot \mathbf{A} \cdot \hat{n} = & \sin^2 i \left(\frac{\partial v_r}{\partial r} \cos^2 \phi + \frac{3v_\phi}{2r} \sin \phi \cos \phi \right) \\ & - \sin i \cos i \left(\left(\frac{\partial v_\theta}{\partial r} - \frac{v_\theta}{r} + \frac{1}{r} \frac{\partial v_r}{\partial \theta} \right) \cos \phi - \left(\frac{1}{r} \frac{\partial v_\phi}{\partial \theta} \right) \sin \phi \right) \\ & + \frac{1}{r} \frac{\partial v_\theta}{\partial \theta} \cos^2 i \end{aligned} \quad (\text{A8})$$

We now must apply some kind of physical prescriptions to the remaining derivatives, which we do in keeping with the Sobolev approximation that there must be *large* velocity gradients present. Using this we approximate the gradients in terms of local escape velocities, i.e. $\frac{\partial v_r}{\partial r} \approx 3\sqrt{2} \frac{v_\phi}{r}$, $\frac{\partial v_\theta}{\partial \theta} \approx \frac{v_{esc}}{(H/R)}$, and $\frac{\partial v_\phi}{\partial r} \approx \frac{\partial v_r}{\partial r}$. Here we assume the local escape velocity is $v_e = \sqrt{\frac{2GM}{r}} = \sqrt{2}v_\phi$ —this would seem to imply that $\frac{\partial v_r}{\partial r} = \sqrt{2} \frac{v_\phi}{r}$, but CM96 adopted an arbitrary extra factor of 3 (seemingly to assume the wind launching regions generate an outflow that travels at a substantial velocity with respect to the source) that we keep to better compare with their results. Since v_ϕ is function of r alone $\frac{\partial v_\phi}{\partial \theta} = 0$, and finally we also set $\frac{\partial v_r}{\partial \theta} = 0$ in keeping with the idea of a geometrically thin disk. This then finally allows us to arrive at the form presented in equation 8 in the text:

$$\hat{n} \cdot \mathbf{A} \cdot \hat{n} \approx \frac{dv_l}{dl} = 3 \frac{v_\phi}{r} \sin^2 i \cos \phi \left[\sqrt{2} \cos \phi + \frac{\sin \phi}{2} \right] - \sin i \cos i \left[3\sqrt{2} \frac{v_\phi}{r} \cos \phi \right] + \cos^2 i \left(\frac{1}{r} \frac{v_{esc}}{(H/R)} \right) \quad (\text{A9})$$

B. FULL PHASE DATA

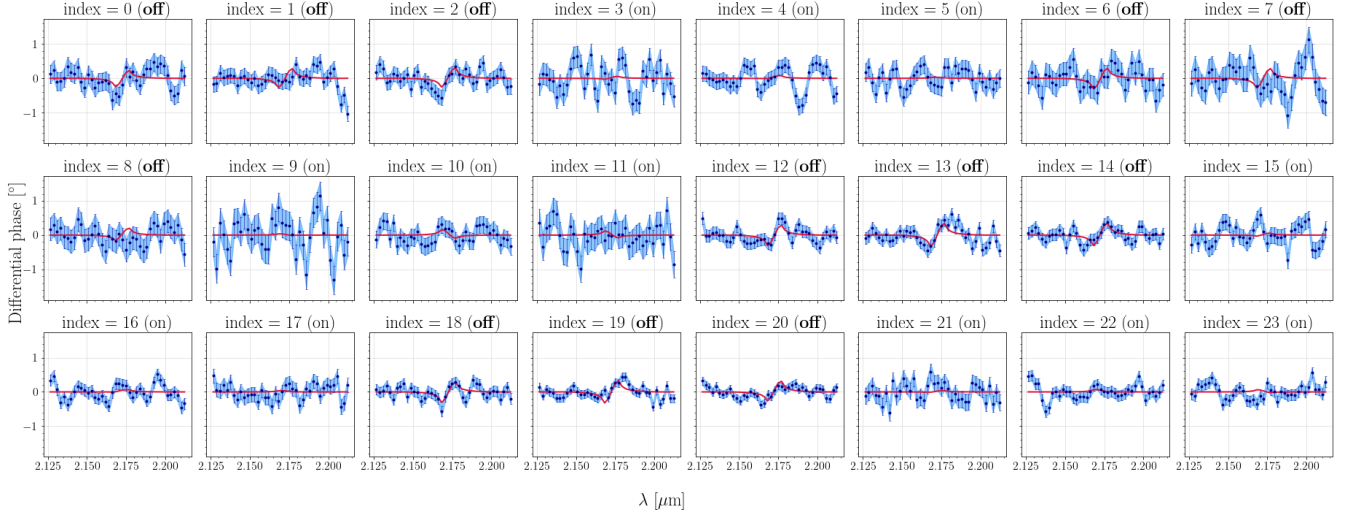


Figure 6. Here we show the individual phase profiles for all 24 possible configurations (6 baselines at 4 epochs). The bold titled “off” axis (from the 3C 273 jet orientation) baselines are the ones that are averaged to create the figures shown in the text. Figure 7 below shows this alignment and why this choice is made. The red lines are the model phases using the average set of parameters given in table 1.

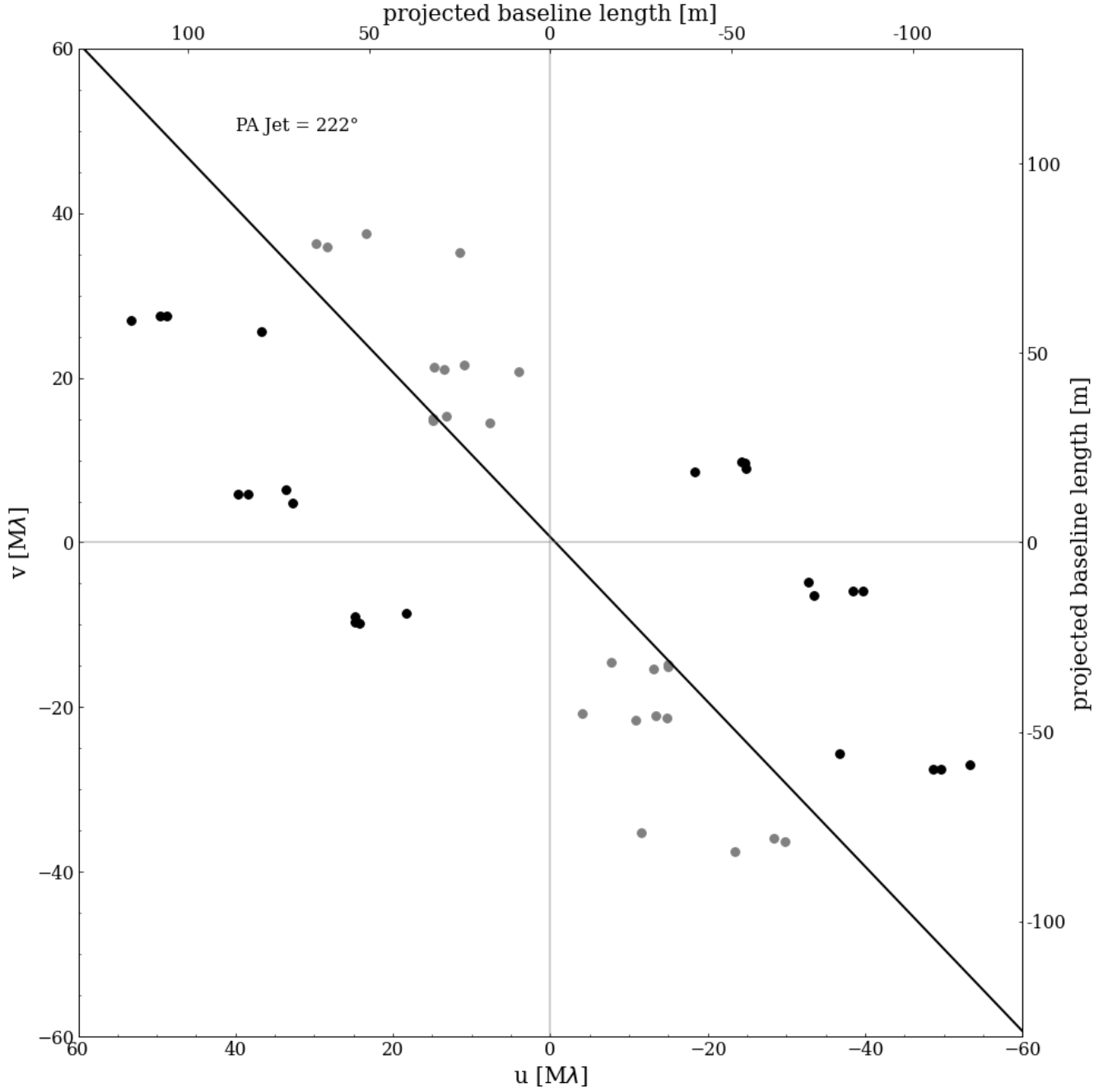


Figure 7. Here we show the baseline and epoch configurations, similar to E1 in [GRAVITY Collaboration et al. \(2019\)](#). The black dots correspond to the bold “off” axis phase plots in figure 6 above, while the lighter grey markers correspond to the “on” axis baselines. We only expect to detect significant asymmetries in the space off of the jet axis, and indeed we observe this, so we only include these off axis baselines in the plots shown in the paper. These on axis baselines are still included in the model, however, so all baselines are fit equally. As shown in figure 6 the fit converges to an essentially flat line in phase space for the on axis baselines as expected for no ordered rotation signature in the jet itself.

C. MCMC DISTRIBUTIONS

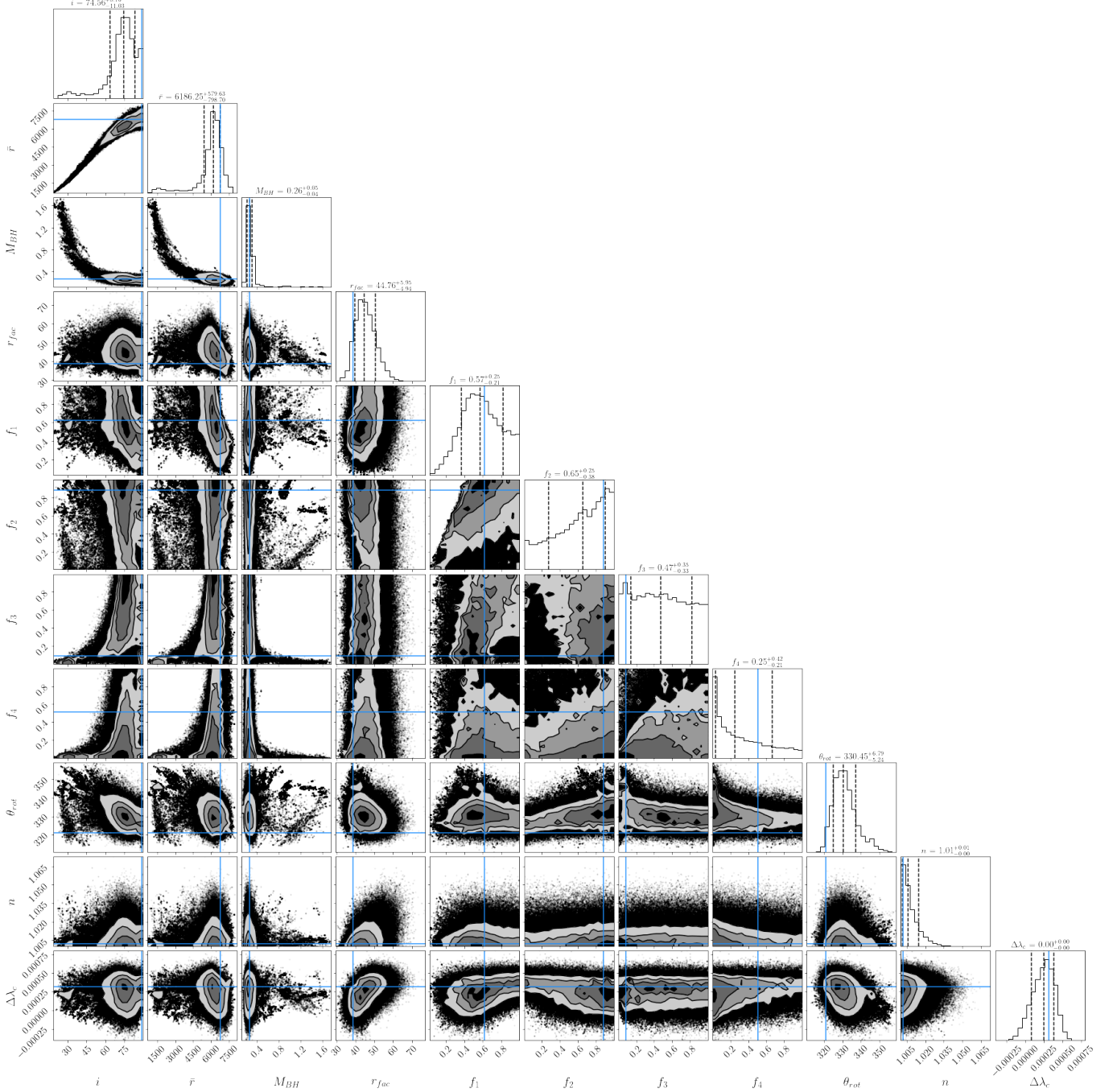


Figure 8. A corner plot showing the regions of parameter space explored and their dependences on one another, with 1D histograms for each. The non-Gaussian shape of the histograms illustrates the importance of using multiple temperatures in the MCMC fitting to ensure the sampler does not get stuck in a local minimum. Also note here that the model uses a rotation convention that is different than the standard PA convention by 90 degrees, i.e. $\theta_{\text{rot}} = \theta_{\text{PA}} + 90^\circ$, and the parameter M_{BH} is in units of $3 \times 10^8 M_\odot$. The blue lines indicate the best fit solution, which is essentially the high inclination model originally considered by Chiang and Murray, but note the difference in the reduced χ^2 between the best fit and the average parameters is only ~ 0.01 . While the various wind launching terms are poorly constrained, it is interesting to note that it appears (from the 1D histograms) that the sampler prefers f_2 approach 1 and f_4 0. f_2 should be 1 in an ideal thin disk, as the Keplerian shear is non-negotiable. f_4 represents a form of isotropic emission which creates a double-horned profile, which means the contributions from it need to be small in order to preserve the observed single peak. The plot was created using Foreman-Mackey (2016).